Results in Engineering 27 (2025) 106649

Contents lists available at ScienceDirect

Results in Engineering

journal homepage: www.sciencedirect.com/journal/results-in-engineering

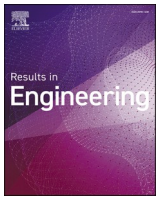

Research paper

K/Ka-band compact low-profile dual differential-fed split ring resonator magnetic-dipole antenna with UWB-frequency-tuning and broad scanning capabilities

Amir Reza Dastkhosh [a,*], Zhong-Xiang Zhang [b], Mehdi Naseh [c], Véronique Moeyaert [c], Fujiang Lin [a]

[a] University of Science and Technology of China, Hefei, China
[b] Hefei Normal University, Hefei, China
[c] University of Mons, Mons, Belgium

ARTICLE INFO

Keywords:
Active phased array antenna
Antenna-in-package (AiP)
Magnetic dipole antenna (MDA)
Satellite communications (SatCom)
Ultra-wideband (UWB)

ABSTRACT

A unique split ring resonator magnetic-dipole (SRR-MD) patch antenna is proposed in this paper. The dual differential-fed SRR-MD antenna boasts a high gain of 8 dB and, in contrast to comparable designs, provides a more compact and low-profile structure. Compared to other designs, this design obtains superior port isolation (>90 dB) and improved isolation between co-polarization and cross-polarization radiation patterns. Furthermore, the antenna provides a broad circularly polarized scanning angle ($\theta = \pm 80^{\circ}$), with a half-power beamwidth and efficiency above 90 degrees and 95%, respectively. The suggested antenna enables ultrawide-frequency tuning, achieving a 67% tuning range, the most among comparable designs which encompasses the whole K/Ka band from 20 GHz to 40 GHz by adjustments to the capacitances of the structure. It has been analyzed, designed, simulated, fabricated, and tested for applications in LEO SatCom mobile terminals, and its circuit model has been presented. The empirical data validate the simulations. The antenna features a compact and low-profile configuration ($0.27\lambda_0 \times 0.27\lambda_0 \times 0.02\lambda_0$) characterized by broadside radiation and dual differential feeding, which enhances its compatibility with power amplifiers (PAs), low-noise amplifiers (LNAs), and transceiver integrated circuits (ICs). This design renders it particularly appropriate for glass-based antenna-in-package (AiP) applications that necessitate the use of thin substrates measuring 300 μm.

1. Introduction

The Internet of Things/Vehicles (IoT/IoV), smart factories, and cities are just a few of the new applications that are causing wireless networks to grow significantly and new generations of communication technologies, like 6 G and beyond, to emerge [1,2]. Satellite mobile communication and new phased array systems for moving objects involves the use of satellite technology to provide connectivity to cars, vessels, aircraft, and other mobile platforms and systems such as navigation, telematics, and infotainment. This type of communication is essential especially in areas where traditional terrestrial networks are unavailable or impractical, for instance, in remote regions, over oceans or in the air. LEO satellites are usually used for internet because they offer lower latency and faster data rates but require a constellation of satellites for global coverage (e.g., Starlink, OneWeb) [3–5]. To achieve ultra-fast data rate, increased connection density and extremely low latency, UWB systems and millimeter-wave (mmWave) technology, new beamforming integrated circuits (ICs), active phased array antenna systems, base stations and user terminal antennas are needed [6–8].

Antenna design is typically conducted independently for 50Ω input and single-ended feeding. In contemporary communication systems, tunable or ultra-wideband scanning antenna arrays in specific frequency bands (K/Ka) and active radio frequency (RF) front-end ICs with differential feeding represent notable advancements. The performance of the system is enhanced, complexity is diminished, energy is conserved, spatial requirements, interconnect paths, and latency are minimized, and the need for multiple narrowband antennas and systems is obviated through co-design techniques such as AiP and system on package (SoP), which are currently under development [8–12]. They will allow the construction of next-generation efficient phased array antennas with

* Corresponding author.
E-mail address: amirreza@mail.ustc.edu.cn (A.R. Dastkhosh).

https://doi.org/10.1016/j.rineng.2025.106649
Received 27 May 2025; Received in revised form 26 July 2025; Accepted 5 August 2025
Available online 7 August 2025

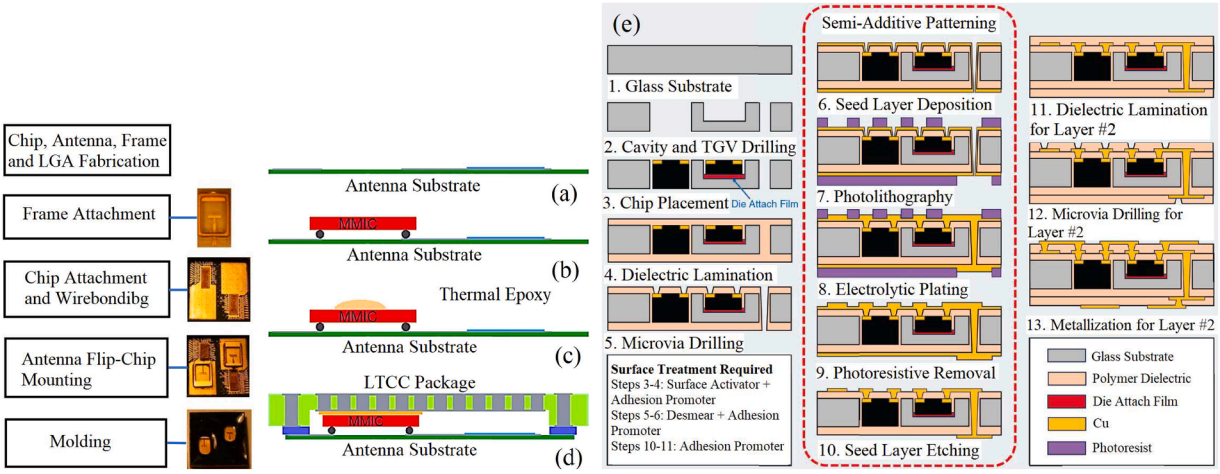

Fig. 1. A sample method of antenna packaging (a-d) and mmWave Glass packaging processes (e) [17–19].

any preferred array configuration wherein the antenna is directly incorporated into the system-level package. Unfortunately, isolation and electromagnetic interference (EMI) are generated. Even though there are methods to enhance the isolation between ports and radiation patterns in certain references [13–15], differential feeding ensures reducing surface waves and the highest level of isolation. This is due to the fact that the midpoint between the two anti-phase signals functions as a virtual ground plane. A small, low-profile antenna featuring minimal volume and broadside radiation, comparable in size to an IC and featuring (dual) differential feeding, is suitable for AiP glass-based packaging. According to Fig. 1, the packaging process for AiP applications is disclosed [16–20]:

i) The antenna substrate is placed onto the substrate holder of the flip chip bonder (a),
ii) The monolithic microwave integrated circuit (MMIC) is flip chipped onto the antenna substrate using a thermosonic (thermocompression and ultrasonic welding) process (b),
iii) Thermal conductive adhesive is dispensed onto the back of the MMIC (c),
iv) The anisotropic conductive film (ACF) is laminated onto the bond pads of the low-temperature co-fired ceramic (LTCC) package,
v) The LTCC package is flip chipped onto the antenna substrate using thermocompression (d),
vi) The applied heat cures the thermal epoxy at the same time,
vii) The entire package is turned around and the cap is attached to it.

The MMIC is situated within the cavity, and a thermally conductive epoxy is utilized between the MMIC and the package base to facilitate heat transfer from the chip to the exterior of the package. This configuration is influenced by the solder ball structures and the thickness determined by the air gap and Glass thickness, thereby enhancing heat dissipation and cooling efficiency.

In AiP, the chip can be connected to the antenna through a grounded coplanar waveguide (GCPW) using flip-chip technology. Conventional packaging procedures and manufacturing technologies can be utilized to offer designers enhanced flexibility. The deployment of AiP necessitates specialized technologies, including LTCC, high-density interconnect technology (HDI), or fan-out wafer-level packaging (FOWLP). Nonetheless, they lead to the creation of multilayered, complex, and expensive antennas that are predominantly suitable for THz frequencies [21–24]. Thinner structures are preferred in AiP for a final merged multilayered stacked module that can simultaneously perform multiple functions, including filtering, amplifying, receiving, and transmitting RF signals. In fact, low-profile structures facilitate improved thermal management by optimizing heat dissipation across multiple layers, resulting in shorter interconnect paths, higher integration density, lower losses at high frequencies, and enhanced electromagnetic compatibility (EMC) through precise layer stacking.

The antenna can be manufactured directly on the same silicon substrate as the integrated circuit (IC). Nonetheless, in AiP and system integration applications, silicon utilized in IC fabrication procedures results in significant losses and exceedingly weak antenna gains (~-8dBi) due to its low resistivity (~10Ω.cm). Consequently, low-loss substrates such as Glass, which offer a range of dielectric permittivity values, are viable choices [25–26]. Glass-based structures and antennas have several merits: they can be applied on moving items, are inexpensive and useful in satellite technology and have incredibly smooth surfaces and good dimensional stability [27]. A Glass substrate would facilitate the integration of optical interconnects directly into the device, eliminating the need for alternative attachment methods. For example, an innovative X-band dual-polarized conformal transparent antenna array with a hemispherical shape and beam coverage, was designed in [28] but is roomy. Notwithstanding the deployment of ultrathin antennas on Glass substrates, along with their miniaturization and low-profile design, as indicated in references [29–37], they fail to encompass (ultra)wide frequency bands and facilitating large scanning angles. Furthermore, end-fire radiation and the single-port-fed mechanism render them inappropriate for large, broad scanning array antennas and AiP applications.

Depending on the application, pitch, diameter, and wafer thickness, two different Glass processing flows are feasible in terms of the limitations of Glass fabrication methods. One process is good for thin wafers (300 μm), while the other is more complicated to construct (double-sided via filling) but enables for processing thicker wafers with greater aspect ratios (by diameter/wafer thickness). The design and implementation of thin, cost-effective Glass substrates with backend packaging technology necessitate low-profile antenna designs. However, they will result in considerable performance deterioration and a decrease in frequency bandwidth of antennas. In this article, the antenna is designed to meet the parameters and constraints for AiP glass-based packaging, encompassing both electrical and geometrical criteria. New features, including a dual-polarized differentially-fed mechanism, UWB-tuning capability, and wide-angle circularly polarized radiation, are introduced by the novel SRR-MD antenna presented here. It is cost-effective, has filtering capability, is smaller and more low-profile than similar designs, and has broadside radiation, in contrast to other magnetic dipoles. Additionally, it accommodates any polarization and the feeding mechanism is differentially designed, with the ability to be directly connected to differential-fed beamformer ICs, differential low-noise amplifiers (LNAs) or power amplifiers (PAs). The theoretical analysis of the suggested high-performance antenna is presented, along

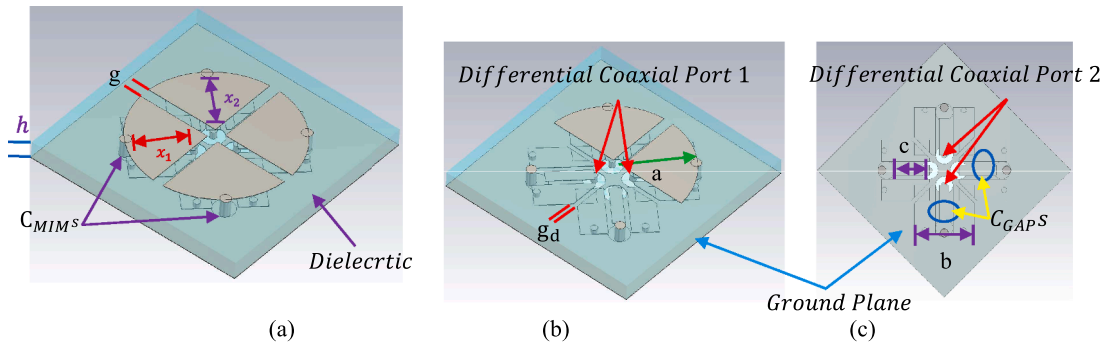

Fig. 2. The geometry of antenna A, dimensions and feeding lines of the proposed antenna and positions of MIM / gap capacitors and VIAs: a) 3D geometry; b, c) dimensions of top and middle layers (dimensions in mm: g=0.2, g_d=0.1, a=1.5, b=1.5, c=1, feed offset = 0.15, substrate thickness h = 0.35, diameter of VIAs: 0.2 and 0.14, distances of VIAs from the center point: 1.5 and 1.6, the gap of MIM capacitors: 0.02).

with its corresponding circuit model. It is analyzed, simulated, fabricated, and measured mainly for use in AiP applications and satellite mobile communications. The analysis of active parameters indicates its superior performance inside the array as well.

2. Proposed dual differential-fed compact split ring resonator magnetic dipole antenna design (SRR-MD)

This section prepares a comprehensive explanation of the design of the proposed SRR-MD antenna. In antenna array design, magnetic dipoles are favored over several other antennas because they generate relatively strong magnetic fields while exhibiting reduced coupling with nearby objects. To avert polarization loss, the suggested antenna must additionally support circular polarization.

2.1. Differential-fed structure and active impedance

The transformation of a differential-fed Hertzian electric dipole into a loop that generates a Hertzian magnetic dipole is a practical and useful technique for our purpose. The differential-fed method reduces distorted emissions and eliminate imbalanced currents on the outside of feed cables effectively. As a result, impedance matching baluns in the external feed cables are no longer necessary. A differential-fed antenna often exhibits symmetric radiation patterns, which is advantageous in phased arrays. Furthermore, differential feeding rejects common-mode noise, has odd linearity if it is matched, and prepares the lowest connections and losses and better impedance matching between IC and the antenna (especially by transformers) [38–39]. The frequency bandwidth and efficiency of the proposed antenna in this work can be further increased by utilizing transformers. A differentially driven antenna can be analyzed of as a two-port network with impedance ratios of two or four. This issue facilitates the process of matching especially for wideband and UWB structures [40–41].

2.2. Limitations of designing low-profile small antennas

Electromagnetic properties and physical limitations and efficiencies of Electrically Small Antennas (ESAs) have been investigated by several authors [42–47]. Chu in [42], calculated and defined quality factor which determines the amount of reactive electric (magnetic) energy stored entirely outside a minimum sphere of radius for an electrically small antenna. Based on Chu theory, we have (s or VSWR = 2):

$$Q_{chu} = \frac{1}{(ka)^3} + \frac{1}{ka};\ BW_{chu} = \frac{s-1}{\sqrt{s}}\left(\frac{1}{(ka)^3} + \frac{1}{ka}\right)^{-1} \quad (1)$$

Therefore, for a typical small antenna with the dimension of ka = 0.5: $Q_{chu} \approx 10$; BW≈7%. Harrington in reference [44], concluded that for having an antenna with high efficiency: ka > 0.5 or a > $\lambda/4\pi$ which 'a' is the maximum radius of the antenna ($k = 2\pi/\lambda$). Recent research [47] investigates the constraints of ESAs concerning certain antennas. These assessments have not been conducted for microstrip antennas or other structures. The area/ surface (S) of a spherical antenna has to be: $(k^2)S = (k^2)4\pi(a^2) > 0.1$, or: $a > \lambda/(4\pi\sqrt{10\pi})$. For a conventional microstrip circular patch antenna, h = (4/3) a ≈ 0.021λ are derived, assuming identical volume. The analysis using ka = 0.2 aligns more closely with the practical values and analyses presented in the referenced materials, yielding: h ≈ 0.044λ (if a= λ/10: h≈0.005λ). Various compact spherical magnetic dipole antennas, including multi-arm spherical helix antennas and spherical SRR antennas, have been developed in several publications [46–50]. Nevertheless, they have been developed for frequencies below 1 GHz, are not differentially fed, exhibit low realized gains and end-fire radiation, and possess dense, heavy, and highly intricate spherical (wire) configurations that make them inappropriate for higher frequency bands. Fortunately, there are certain techniques for antenna miniaturization, such as metamaterial structures [53–55]. However, all of them operate at significantly lower frequencies, lack (dual) differential feeding and wideband capabilities, are bulky and thick, and challenging to manufacture. Moreover, they lack sufficient or high isolation [56–57].

2.3. Antenna analysis and design

Typically, the optimum lengths and widths for a planar conductor of an antenna to resonate are between λ/2 and λ/4. As previously mentioned, the frequency bandwidth and efficiency of an antenna will be diminished as a result of the reduced antenna height and size. However, in applications such as AiP and glass-based packaging, thin or compact low-profile structures are preferred (h = 300 μm).

In order to guarantee a symmetric and stable boresight pointing radiation patterns and within the operating band, differential feeding is used to excite the perfectly symmetrical radiator. Also, circular polarization can be more effectively prepared by a circular antenna structure. Figure 2 depicts the geometry and dimensions of the designed antenna. The thin circular microstrip antenna can be analyzed by cavity model [58–59]. The principal excitation structures are formed by the current loops with shorting VIAs, which function as differential-fed magnetic dipoles. Each differential-fed antenna demonstrates nearly independent radiation characteristics as a consequence of the excitation mechanism, which leads to minimal and negligible mutual coupling and maximum isolation with another antenna. The differential-fed technique excites the TE_{11} mode (fundamental mode) within the antenna cavity, since the feeding points are positioned along the central axes of the structure, generating surface currents or electric fields along these lines (as will be demonstrated in the subsequent section). It also allows for the excitation of just half or fewer of the modes which are at least twice as high (odd linearity). The radiation of all modes reaches the peak in the broadside

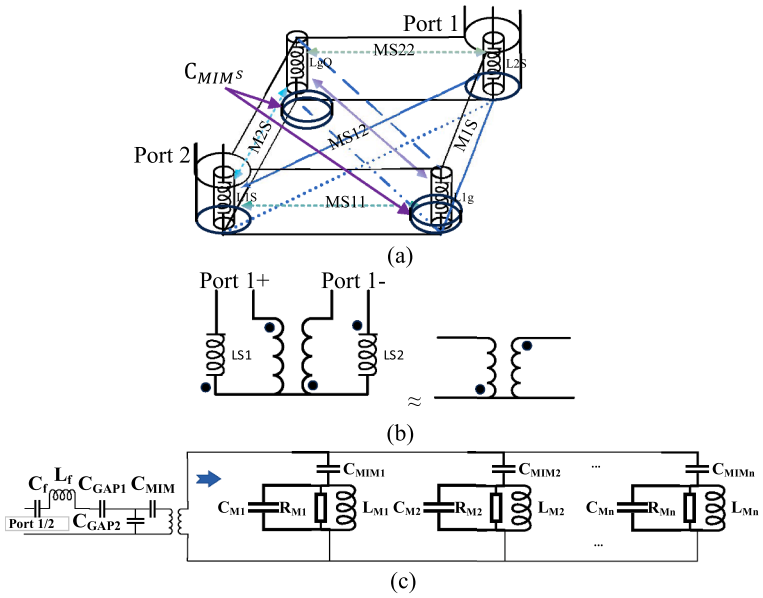

Fig. 3. a) Modeling VIAs of the proposed antenna [59] (circuit model for two signal VIAs sharing ground VIAs) and C_{MIM} positions, b) combination of ground VIAs and two differential signal VIAs into equivalent self-inductances and mutual inductance, and c) circuit model of the proposed antenna with SRRs for each port.

direction and the radiations of all even modes are suppressed in all directions and the radiation patterns in the E- and H-planes are almost similar. In our design, assuming $a = 0.15\lambda_0$, $h = 0.02\lambda_0$ and $\varepsilon_r = 2.5$, the minimum resonant frequency for a circular patch antenna with a = 1.8 mm will be: $(f_r)_{110}^{TE^z} \approx 30$GHz (a and a_e are the values of actual radius and effective radius of a circular patch antenna). But due to the suggested antenna configuration discussed in the subsequent paragraphs, the antenna is capable of resonating at lower frequencies. In the designed circular differential-fed antenna, the feeds points are positioned at points (ρ_1, ϕ_1) and (ρ_2, ϕ_2), respectively ($\rho_1 = \rho_2$ and ϕ_2 - $\phi_1 = \pi$). The differential input impedance for each port of the cavity is determined by employing cavity analysis at a single resonant frequency and disregarding any inductors and capacitors in the structure [39]:

$$Z_d = -2j\omega\mu h \sum_{m=1}^{\infty} \times \sum_{n=0}^{\infty} \frac{\epsilon_0 n}{\pi} \left\{ \left[j_0\left(\frac{n\phi_\omega}{2}\right) \right]^2 \frac{J_n^2(k_{nm}\rho_1)}{J_n^2(k_{nm}a_e)} \times \frac{k_{nm}^2 \cos^2(n\phi_1)[1-\cos(n\pi)]}{\left[k_0^2\epsilon_r(1-j\delta_e)-k_{nm}^2\right]\left(k_{nm}^2 a_e^2 - n^2\right)} \right\} \quad (2)$$

where n is the mode index in the ϕ direction, ϕ_ω is the effective width of the feed that needs to be chosen to obtain good agreement between the theoretical and experimental impedances, δ_e is the effective loss tangent and $\epsilon_{0n} = 1$ for n = 0, $\epsilon_{0n} = 2$ for $n \neq 0$. At the resonance frequency of a differential circular patch antenna, the input impedance is approximately 200Ω. Eq. (2) delineates the cancellation mechanism of the differential excitation, too ($1 - \cos(n\pi)$ multiplier). Several parallel MD-SRRs, which are composed of magnetic dipoles, inductors, and capacitors, are simultaneously excited by the feeding structure to achieve wider impedance matching. The capacitances are formed by metal gaps and metal-insulator-metal (MIM) capacitors situated between the feed lines and the ground plane or radiating patches. Capacitances can also be generated using metal-oxide-semiconductor (MOS) or lumped capacitors. The inductances are generated by VIAs and/or thin transmission lines.

The antenna circuit model is depicted in Fig. 3, which elucidates the impact of the capacitors and inductors mentioned on ultimate resonant frequency and bandwidth of the antenna. It offers a clearer perspective for tuning and optimizing the antenna, leading to minimized or specified antenna dimensions with maximal efficiency and bandwidth. The antenna for each differential port includes a transformer and consists of two magnetic dipoles with equivalent coupling values and orientations. Due to the differential feeding of the antenna, the isolation values between the two differential ports are expected to be perfect or infinite. Coupled lines have been employed for antenna feeding to enhance impedance matching and efficiency. MIM/gap capacitors can be calculated by [60–61]:

$$C_{MIM} = \frac{\varepsilon_r S}{4\pi k h_m};\ C_{GAP} = \frac{\pi\varepsilon_r w}{ln\,(g/t)} \quad (3)$$

where S is the area of the MIM capacitor, h_m is the thickness of the dielectric between the plates of the MIM capacitor, l is the total length of each resonator, w is the width of the resonator/metallic sheet (here the average widths of the radiating patches), g is the gap distance of the Gap capacitor and t is the thickness of metal strip. MIM capacitors provide a higher capacitance value and a reduced size relative to interdigital capacitors. VIAs facilitate the ingress of current and field into the cavity. The inductors formed by VIAs or thin transmission lines are computed using:

$$L_1 = \frac{\mu_0}{2\pi}\left[h\ln\frac{h+\sqrt{h^2+r^2}}{r} - \sqrt{h^2+r^2} + \frac{h}{4} + r\right] \quad (4)$$

where, L_1 represents line inductors including VIAs and r is the radius of shorting VIAs. The values of inductors created only by VIAs and coupling effects between them can be calculated by [62]:

$$L = \frac{\mu_0 h}{2\pi}\left[\ln\left(\frac{x_1+x_2}{4(r)}\right) - 0.75\right];\ M = \frac{\mu d}{2\pi}\left[\ln\left(\frac{x_1+x_2}{4(s_{1k}+r)}\right) - 0.75\right] \quad (5)$$

where x_i are the geometrical dimensions of feed that excites the antenna or the distances among feed points (ports) and grounded VIAs (Fig. 2a), s_{1k} are the distances between the signal VIAs and d is the distance among grounded VIAs. L is created by VIAs and affected by their dimensions and M is created by mutual coupling between VIAs. The mutual couplings between VIAs function as transformers, enhancing impedance matching, while their positions and dimensions influence the final scattering characteristics of the antenna. The overall inductance is determined by the sum of series and parallel inductances, with increased inductance arising from a diminished number of inductors conFig.d in parallel (Fig. 3 b, c). The incorporation of extra capacitors, along with

Table I
Comparison Of Current Work With Previous Designs.

Ref.	Type	Bandwidth (GHz) / (%)	Element Size $(\lambda 0)^3$	Peak Gain; (dB) Efficiency (%)	HPBW: H/E	Pol.[1]	Process/ Feeding/ Suitable for AiP or GBP[2]	Isolation: Between Ports; R.P.[3] (dB)	DF/ Tun.[4] (%)	R.P.	S.A.[5]	NL[6]
[51]	SIW-MD[7]	16-16.5 / (3)	0.72 × 0.72 × 0.08	2.7; 85 ($\varepsilon_r = 2.5$)	80/80	LP/V.	PCB / MS/ No	S.P.[8]	No/No	E.F.[9]	NA	1
[52]	MS-MD[10]	24-30 / (22)	0.7 × 0.45 × 0.07	6; 90 ($\varepsilon_r = 2.5$)	100/NA	LP/V.	LTCC[11] / MS/ No	S.P.	No/No	E.F.	NA	1
[64]	MS-MD	2.38-2.51 / (5)	2.9 × 1.17 × 0.025	13; 80 ($\varepsilon_r = 1$)	30/100	LP	PCB / MS/ No	S.P.	No/No	B.S.[11]	NA	2
[80]	SIW-SRR	24-28.6 / (17.5)	0.28 × 0.28 × 0.17	6.2; NA ($\varepsilon_r = 6$)	80/90	LP	PCB / SIW/ No	NA; 20	No/No	B.S.	±55°	3
[81]	SRR	3.3-3.8 / (14)	0.23 × 0.23 × 0.04	4.7; 83 ($\varepsilon_r = 2.2$)	NA	Dual	PCB / Slot/ No	20	No/NA	B.S.	NA	3
[82]	SRR	0.902-0.928 / (3)	0.21 × 0.21 × 0.03	5.7; 91 ($\varepsilon_r = 2.2$)	NA	LP/CP	PCB / Coaxial/ No	SP	No/(25)	B.S.	±30°	2
[83]	SRR	3.3-3.8 / (14)	0.28 × 0.28 × 0.03	5.4; 77 ($\varepsilon_r = 2.2$)	94/90	CP	PCB / MS/ No	15	No/(10)	B.S.	±30°	3
[84]	Patch	4.8-5 / (4)	1.3 × 1.3 × 0.05	9.6; NA ($\varepsilon_r = 3.5$)	80/40	Dual	PCB / Coaxial/ No	60	Yes/No	B.S.	NA	1
[85]	Patch	3.3-3.6 / (9)	0.29 × 0.29 × 0.06	8; NA ($\varepsilon_r = 2.7$)	70/70	Dual	PCB / MS/ No	35	Yes/NA	B.S.	NA	3
[86]	MS-Slot	8.4-8.8 / (5)	0.9 × 0.9 × 0.023	3; NA	70/100	Lin.	PCB / Slot/ No	SP	No/No	B.S.	±90°	2
[87]	SIW-SRR	2.45-2.75 (12) 3.5-3.8 (8)	0.48 × 0.4 × 0.02	3.6 3.15	75/95	Dual Lin	PCB / SIW/ No	20	No/(12)	B.S.	NA	1
[88]	MED[12]	25-43 / (53)	0.4 × 0.4 × 0.12	5	70/80	Lin.	FOWLP/ Coaxial/ Yes	SP	No/No	B.S.	±55°	5
This Work	SRR-MD[13]	B: typ.: 27-30 (20-40) / (10) A: typ.: 25-27 (20-40) / (10) typ.: 28-28.5 (24-34) / (2) typ.: 17.9-18.4 (15-25) / (3)	0.27 × 0.27 × 0.02 0.25 × 0.25 × 0.025 0.2 × 0.2 × 0.022 0.2 × 0.2 × 0.02	7; 96% ($\varepsilon_r = 2.5$) 8; 94% ($\varepsilon_r = 2.5$) 2.5; 85% ($\varepsilon_r = 6$) 3; 80% ($\varepsilon_r = 6$)	80/90 90/100 110/120 115/120	Dual	PCB / GBP[13] Coaxial/ Yes	90; 80/30 (LP/CP)	Yes/(67)	B.S.	±80°	2; 3[14]

Pol.[1]: Polarization; GBP[2]: Glass-based Packaging; R.P.[3]: Radiation Pattern; DF/Tun.[4]: Differential-Fed/Tunable; S.A.[5]: Scanning Angles; NL[6]: Number of Layers; SIW-MD[7]: Substrate Integrated Waveguide Magnetic Dipole; S.P.[8]: Single Port; E.F.[9]: End-Fire; MS-MD[10] : Microstrip Magnetic Dipole; B.S.[11]: Broadside; SRR-MD[12]: Split Ring Resonator Magnetic Dipole;; MED[13]: Magneto-Electric Dipole; 3[14]: Three Layers with MIM Capacitors.

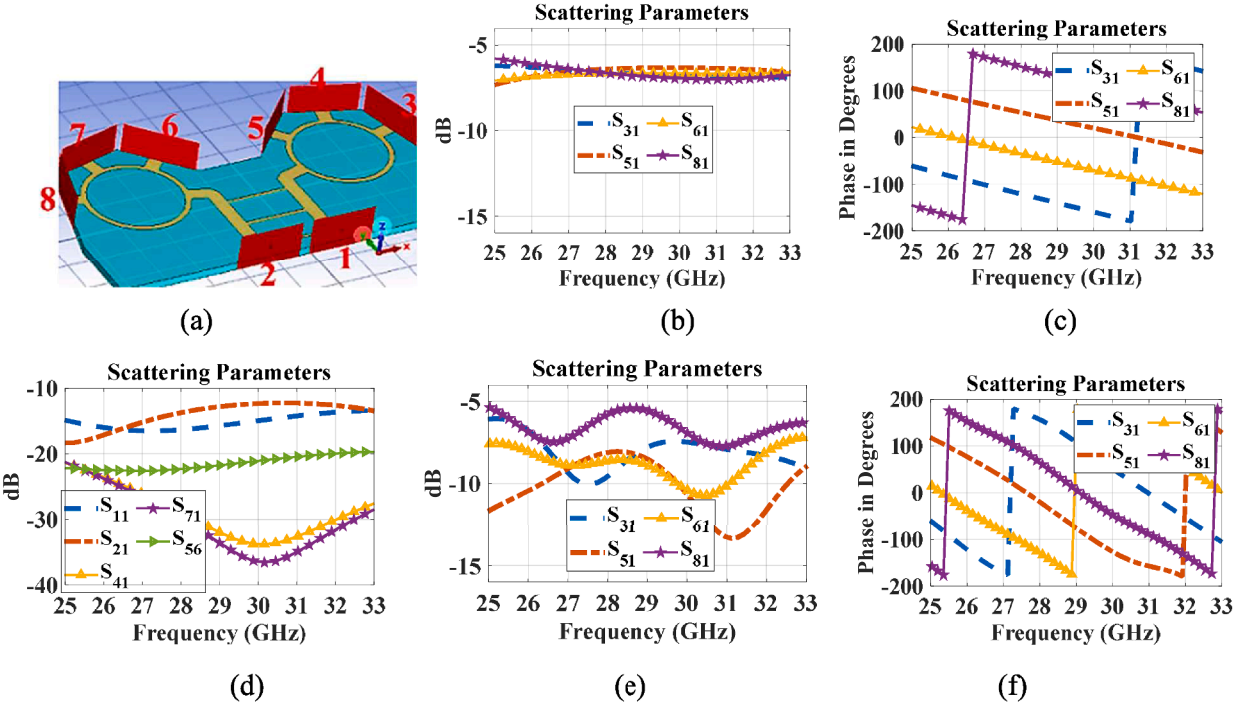

Fig. 4. A typical designed eight-port hybrid phase shifter and its specifications separately without connection lines (a, b, c, d); and based on PCB properties (e, f).

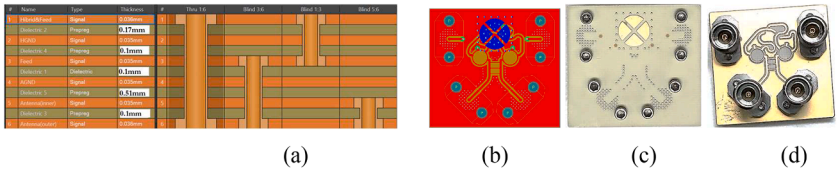

Fig. 5. A typical multilayered PCB with antenna D and test board or hybrids: a, b) PCB in Altium Designer; c) top layer and d) bottom layer of the fabricated PCB with 2.92 connectors.

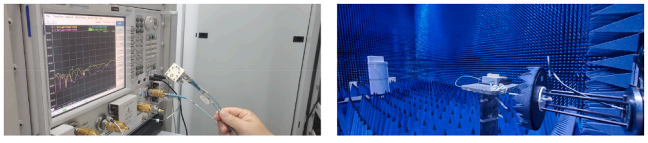

Fig. 6. a, b) antenna under test in antenna chamber for radiation pattern measurements by near-fields to far-fields transformations.

the correct quantity and dimensions of VIAs, attains the necessary reduction in resonance, hence minimizing the electrical size of the antenna. The ultimate resonant frequency of the SRRs is found by [63]:

$$f_r = \frac{1}{2\pi\sqrt{L_t C_t}} \tag{6}$$

which L_t and C_t define the total capacitance and inductance of the structure. The designed antenna configuration comprises six parallel VIAs and two parallel MIM capacitances at each differential-fed port SRR-MD. Therefore: h = 0.3 mm, r_{avg} = 0.1 mm (r_{avg} is the average radius of the grounded VIAs of each loop); $L_t \approx L \approx L_1/6 \approx 10$pH, $C_t \approx 2 \times C_{MIM} \approx 7$pF: (f ≈ 20 GHz). A dual differential-fed antenna structure with four current loops is developed to accomplish dual polarization. The design procedure of the proposed antenna can be outlined as follows:

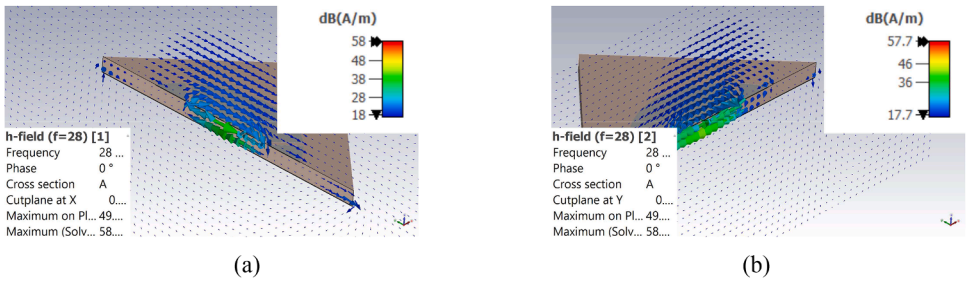

Fig. 7. Magnetic fields show the creations of the magnetic dipoles in the middle of each arm of the antenna B @ 28 GHz at: a) port 1, b) port 2.

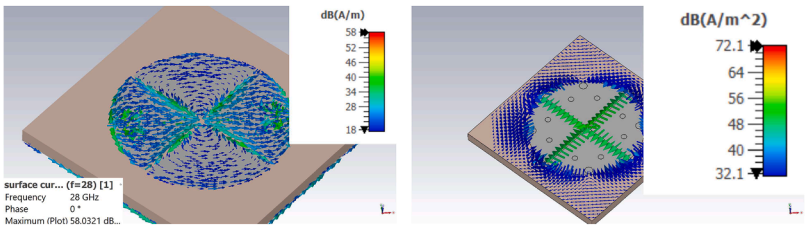

Fig. 8. Surface current (a), and current density (b) at port 1 @ 28 GHz (antenna B).

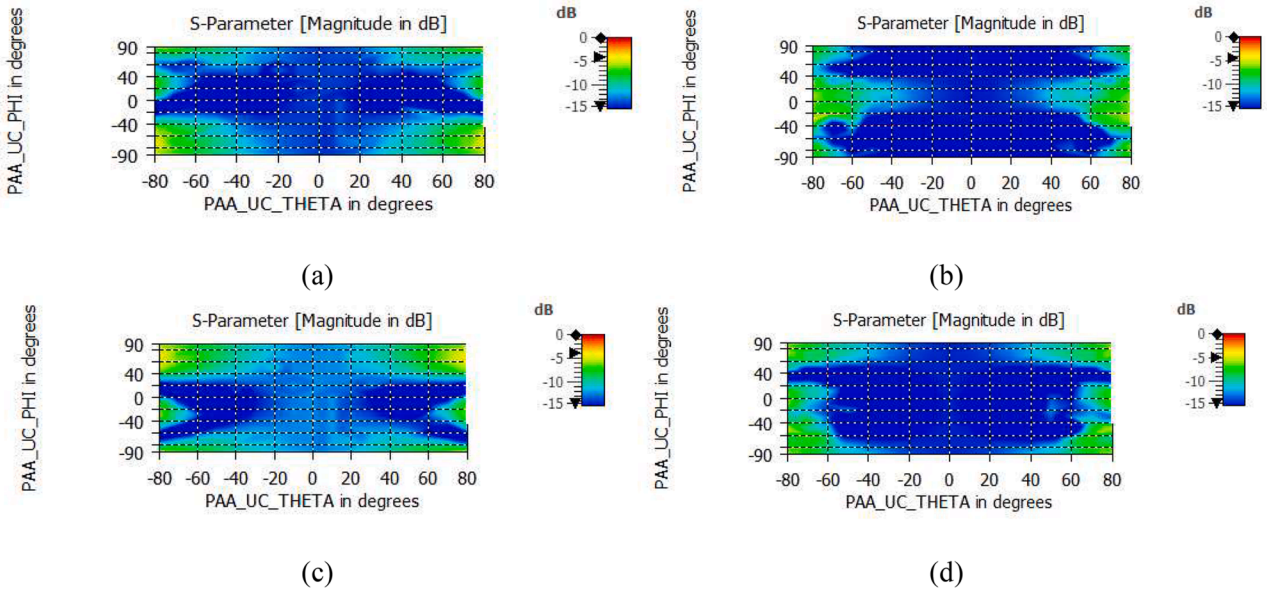

Fig. 9. Active reflection coefficient and isolation (in dB), @ 28 GHz (a, b) and @ 29 GHz (c, d).

a) calculating the size of the circular patch antenna using an appropriate feeding mechanism (coupling through feeding lines),
b) design a differential-fed port configuration,
c) incorporate inductors and capacitors in the MD loops,
d) adjustment of parameters/dimensions using CST Studio Suite to attain a high-performance antenna,
e) develop a dual-port differential-fed antenna and implement final improvements and adjustments.

Image theory suggests that the height of a printed electric dipole antenna should approximate one-quarter of the wavelength; yet, the designed antenna can produce omnidirectional radiation patterns in the top half-space when constructed on extremely thin substrates. In the proposed antenna, metallic shorting VIAs connect each patch arm to the ground, and in conjunction with the ground plane, they create a center-fed loop antenna. The capacitances of the MIM/gap capacitors and the inductances/mutual coupling of VIAs enhance the adaptability of the resonant frequency and improvement of impedance matching of the antenna. This horizontal SRR-MD antenna, as outlined in the subsequent section, delivers a broader impedance bandwidth as a result of its UWB-frequency-tuning capability, broadside and wide circularly-polarized radiation, more compact dimensions, and superior performance as a result of its unique design [64–66] (also Table I).

3. Simulations and measured results

This section clarifies the simulation and empirical findings. A hybrid 8-port phase shifter has been developed for antenna evaluation. Fig. 4 illustrates the parameters of the hybrid. The antenna and hybrid are integrated to form multilayered PCBs. Ultimately, to improve isolation between two differential ports and their feeding, microstrip lines should be utilized alongside striplines. Despite the transmission line lengths from the hybrid outputs to the antenna input ports were precisely calibrated using the "interactive length tuning" feature in Altium Designer and were identical, we observed discrepancies in the phases and amplitudes at the antenna input terminals compared to the simulations. This was attributable to the differing configurations of the transmission or connection lines, leading to variations in inductances and capacitances of the transmission lines (Fig. 4 e, f). Several authors have developed hybrid phase shifters in the references [67–69]. However, they consist of intricate and expansive constructions with several transmission lines and stubs, requiring extended transmission lines for connection to antenna ports. Consequently, they generate increased losses and phase discrepancies or diminished accuracies. Utilizing highly accurate, calibrated, and optimized test boards or beamformer ICs capable of generating precise and/or adjustable phases and amplitudes with minimal lengths, will enable measurement results to align closely with simulation outcomes.

The test facilities and the fabricated multilayered antenna structure, which is combined with a hybrid phase shifter, are illustrated in Figs. 5-6. Glass substrate (loss tangent = 0.009, $\varepsilon_r = 2.6$) and Rogers RO4350 substrate (loss tangent = 0.002, $\varepsilon_r = 3.6$) were utilized to design and fabricate four distinct antennas in alignment with the specified requirements, available substrates, and manufacturing technologies [25–26]. Antennas A and B possess SRRs with distinct optimum dimensions and were designed on Glass substrate. Antenna A possesses

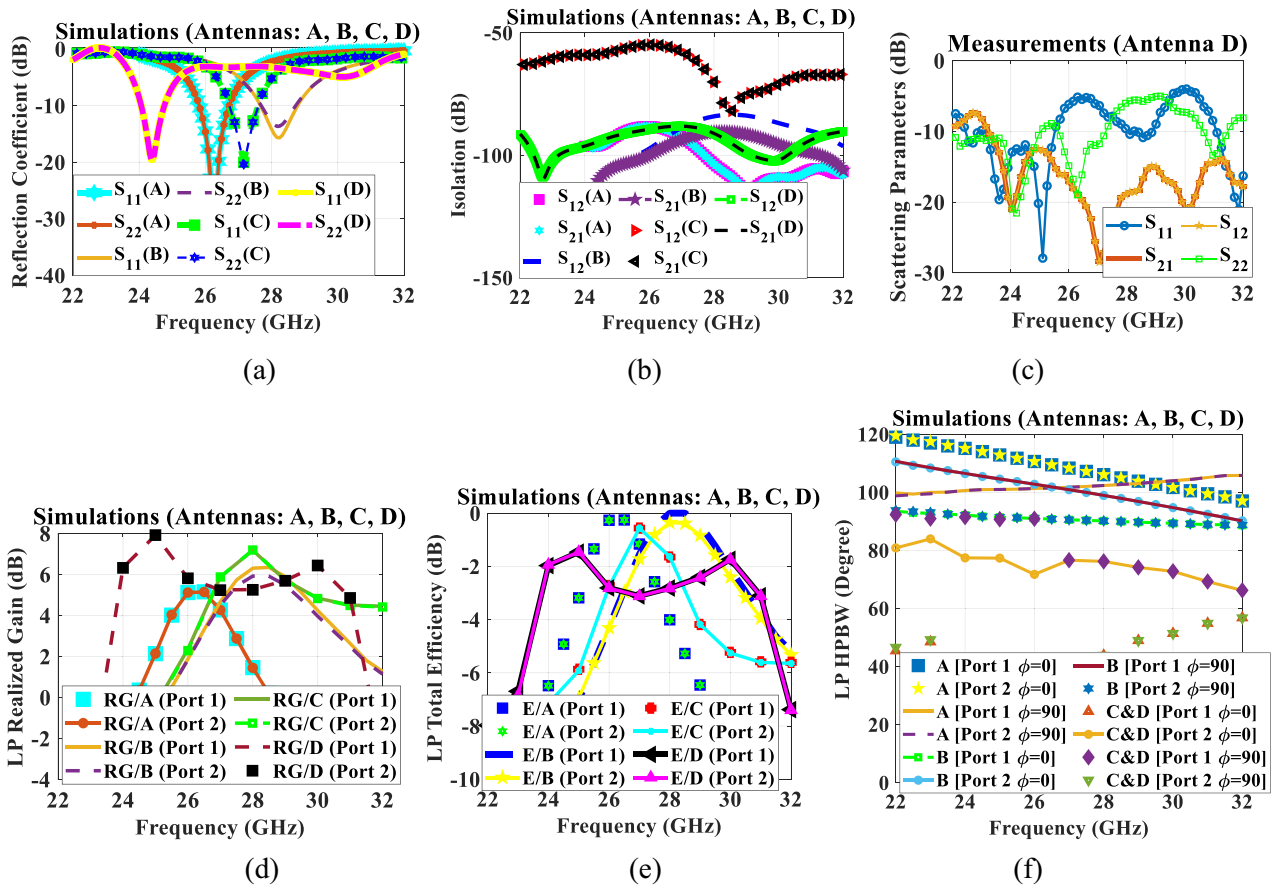

Fig. 10. Simulated scattering parameters of the antennas (a, b); measured results of reflection coefficients and isolations for antenna D (c); simulated linearly polarized realized gain and efficiency of the antennas (d, e); HPBW (f).

larger MIM and Gap capacitors than antenna B. Antennas C and D do not incorporate SRRs and possess the fewest Blind VIAs. Antenna C was designed on Glass substrate, whereas antenna D was designed and fabricated using Rogers RO4350. The dimensions of the antennas are: A: 3.2 × 3.2 × 0.35mm^3; antenna B: 3.9 × 3.9 × 0.3mm^3; C: 7 × 7 × 0.35 mm^3; D: 7 × 7 × 0.6 mm^3.

The specifications of the antennas in the most compact and low-profile designs (antennas A, B), as will be demonstrated in the subsequent paragraphs and Figs, are highly sensitive to the dimensions and substrate properties, or consequently, to the fabrication technology and the materials employed. The differential port centers are situated in close proximity (0.75 mm), complicating impedance matching and feeding, particularly for testing purposes. A mere 0.01 mm alteration in the size of MIM capacitors can result in an approximate 0.25 GHz frequency variation (at 30 GHz). Utilizing a substrate with $\varepsilon_r = 3.6$ instead of $\varepsilon_r = 2.6$ will result in an approximate frequency shift of 5 GHz, leading to a lower resonance at 25 GHz instead of 30 GHz. Furthermore, the diameters of some (Blind) VIAs in the intermediate layer fall within the range of 0.1 mm, rendering their implementation unfeasible due to constraints in available fabrication technology (the smallest achievable VIAs are 0.15 mm with 0.1 mm edge-to-edge spacing).

Detailed explanations of these issues are provided in the following sentences. On Glass substrates and available fabrication technology, additional constraints exist, including the use of Blind vias and multi-layered PCBs, when the Glass thickness is restricted to 0.3 mm. The implementation of MIM or lumped capacitors is another issue, as seen in Figs. 2 and 3. The antenna be constructed on alternative available substrates, including S1000H UL ANSI: FR-4.0 (high-performance FR-4.0). However, its permittivity is elevated at 1 GHz (4.6) and is inappropriate for the intended mmWave applications due to its high loss tangent, which considerably impairs the efficiency of the antenna (0.011 at 1 GHz and 0.025 at 10 GHz). In addition, the minimum thickness of 0.05 mm is insufficient for the implementation of MIM capacitors (0.02 mm is required). Rogers RO4350B substrate is capable of supporting multilayered PCBs with a minimum thickness of only 0.1 mm. Other fabrication technology limitations for Rogers RO4350B substrate included the following: a minimum hole size of 0.15 mm (0.1 mm is required), a minimum distance of 0.2 mm between the VIA hole and conductive pattern (0.1 mm is required), a minimum back drill layer thickness of greater than 0.15 mm (0.1 mm is required), a minimum back drill diameter of 0.3 mm (0.1∼0.2 mm is required), and a minimum space of 0.2 mm between back drilling or Blind VIAs and transmission lines (back drilling is a technique used to implement Blind VIAs). Consequently, certain thicknesses and values were altered or increased, and some Blind VIAs were converted to Through VIAs due to these constraints [70]. Thus, a modified antenna D was implemented on the RO4350B Rogers substrate (Epoxy/Glass processes) for the fabrication and testing. This antenna is larger and simpler to fabricate, with larger VIAs and distances between ports, as well as wider connection lines and a wider frequency bandwidth. The accuracy of measurements was influenced by the further modification and tuning of the new structure. Epoxy/Glass processes were used to prepare the fabrication technology of Blind VIAs and the implementation of multilayered PCBs.

The Anhui Engineering Research Centre for Microwave and Communications, located at Hefei Normal University in Hefei, China, conducted the antenna testing. The network analyzer utilized was the Agilent PNA-X N5247A. The antenna was evaluated at certain frequencies according to the frequency bandwidth of the hybrids. Discrepancies between simulation results and fabrication outcomes are affected by fabrication accuracy, insufficient isolation among test board

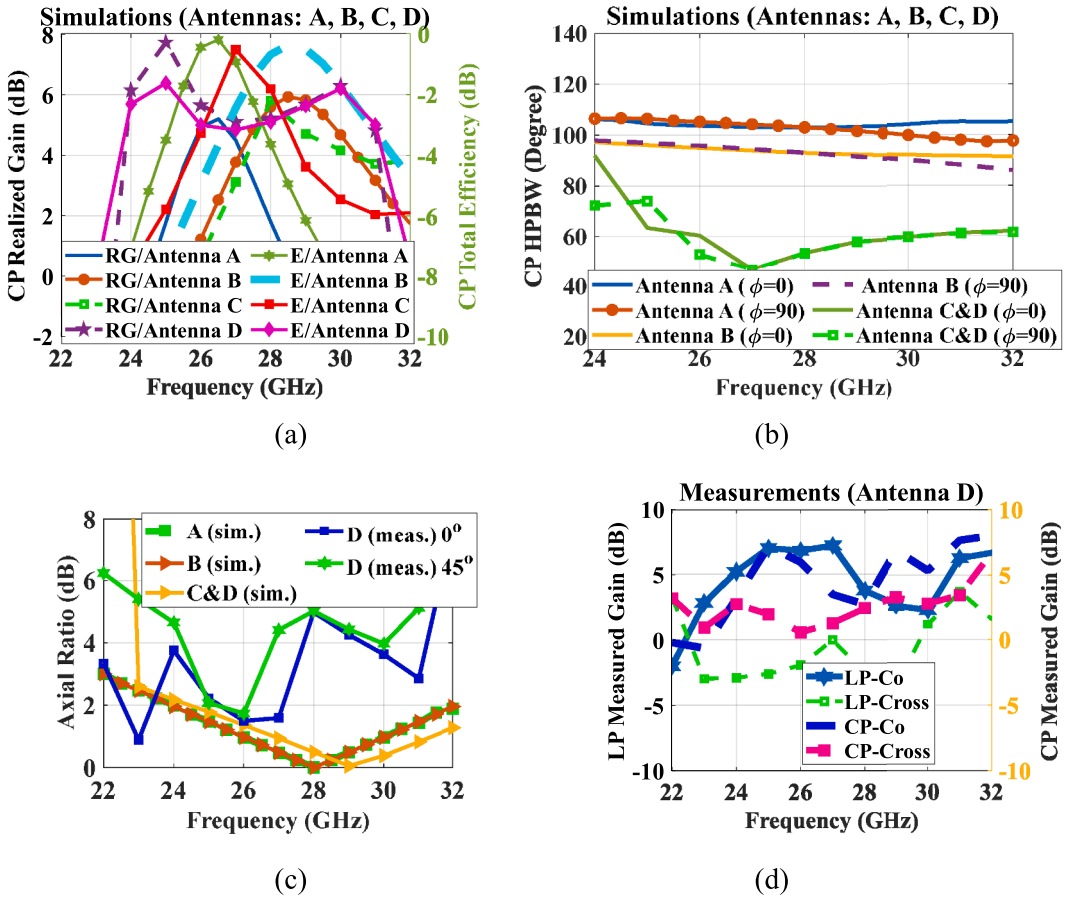

Fig. 11. Simulated circularly-polarized realized gain/RG and efficiency (a), and HPBW (b) for antennas A, B, C; c) simulated and measured axial ratios, and d) measured linearly and circularly polarized realized gain of antenna D.

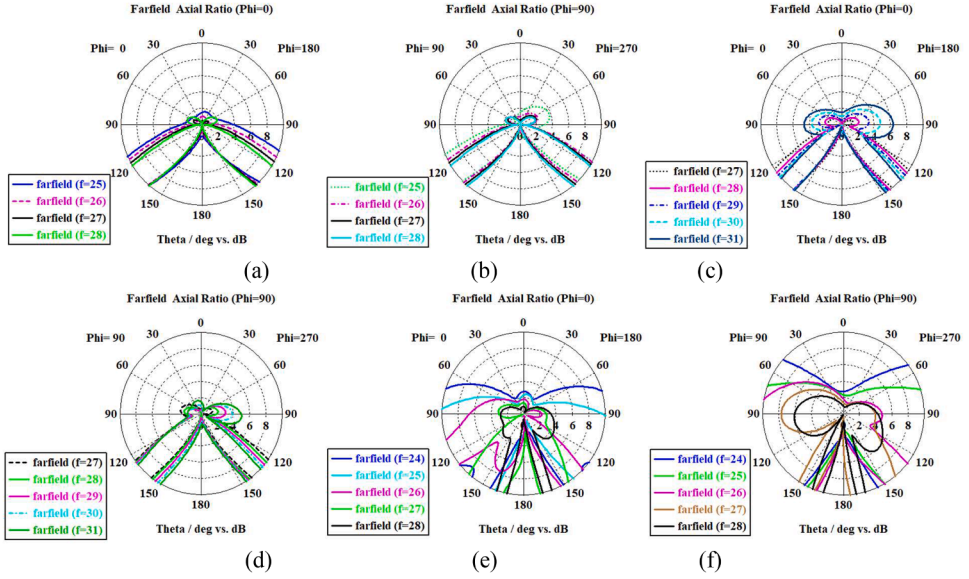

Fig. 12. Axial ratio beam patterns of the proposed antennas for antenna A (a, b), antenna B (c, d), antenna C, D (e, f).

ports (particularly the 90-degree hybrid phase shifter), connector radiation and placement effects, measurement inaccuracies of the testing apparatus (up to approximately 2 dB, according to the datasheet from NSI-MI Technologies and the test operator's report), frequency deviations and inaccuracies in the phase and amplitude of the hybrids. Antenna testing, specifically near-field to far-field transformation, evaluates far-field properties of an antenna by measuring its near-field patterns within a chamber. This obviates the requirement for an expansive, open-area testing location, thereby enhancing the efficiency of antenna evaluation. The capacity of the system to precisely convert

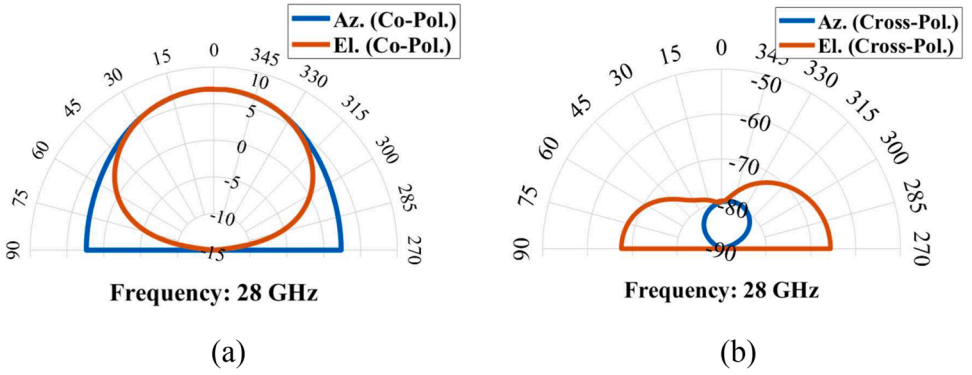

Fig. 13. Simulated co and cross polarization radiation patterns at linearly-polarized mode for antennas B.

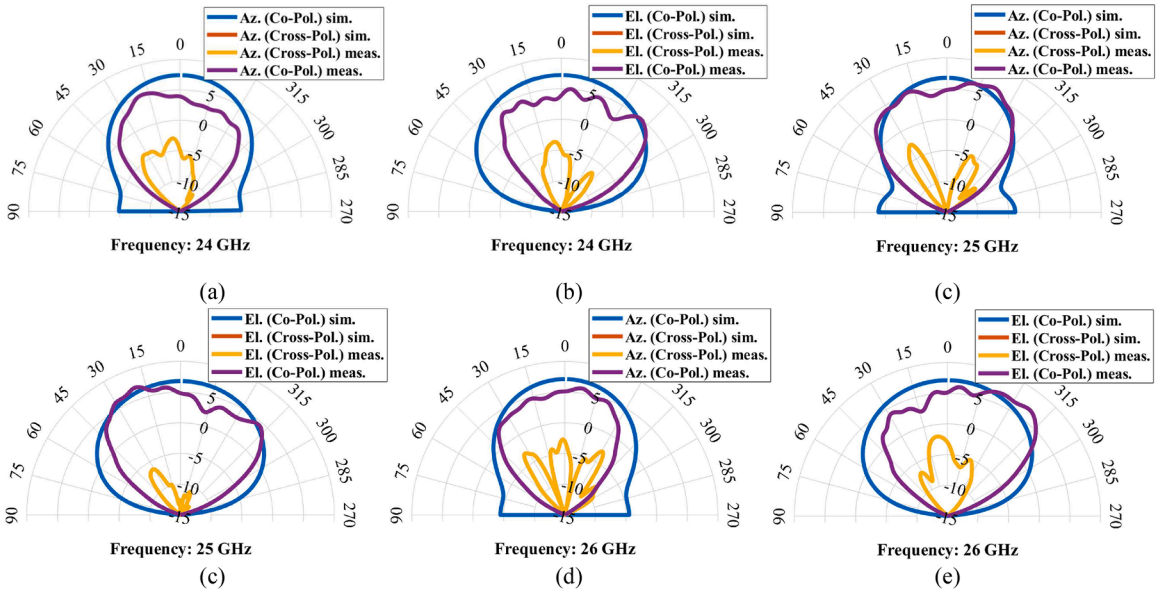

Fig. 14. Simulated and measured co-/cross-polarization realized gain radiation pattern for linearly-polarized mode at different frequencies for antenna D.

near-field data into far-field results depends on the calibration method. It commonly comprises three steps: a) probe calibration, b) system calibration, and c) post-processing calibration. Initially, the probe is calibrated in free space using a standard antenna, such as a reference dipole or horn antenna with a specified radiation pattern. The near field of the standard antenna is assessed to verify the precision of the probe. Subsequently, system calibration is performed. The complete measuring apparatus undergoes testing during system calibration utilizing a reference antenna with established far-field patterns. It also ensures scanner accuracy (e.g., robotic arm or planar scanner) with laser trackers or encoders. Finally, to post-process near-field sensor data, NF-FF transformation software is employed. This step verifies that the data aligns with the patterns of far-field radiation by comparing the NF–FF converted pattern with the known far-field results. Periodic calibration be required to account for shifts or environmental changes that might affect data, such as temperature or humidity [71–72]. The conversion of the rectified near-field data to the far-field is accomplished via techniques and algorithms implemented by NSI-MI Technologies.

Figs. 7-16 depict the simulated and measured results of the proposed antenna. Fig. 7 illustrates the formation of magnetic dipoles at the midpoints of the arms of each differentially-fed magnetic dipole ($x = y = a/2$). For each differentially-fed SRR-MD, the total magnetic fields result from the amalgamation of the magnetic fields from both arms, which are oriented in the same direction. As explained in the previous section, the differential-fed mechanism excites TE_{11} mode. Fig. 8 shows the surface currents and current density at typical port 1 that proves the excitation of the fundamental TE_{11} mode. Mutual coupling and/or surface waves result in scan blindness [73]. A substrate characterized by low dielectric permittivity and reduced height is essential for the effective attenuation of surface waves. The differential-fed mechanism of the antenna markedly diminishes surface waves, particularly those produced by even modes, as demonstrated in Eq. (2). Therefore, active parameters are crucial in the antenna analysis and design. The active element parameters are determined in an antenna array when all input voltages are set to zero and all ports are loaded and matched, with the exception of the nth port, which is set to unity [74–75]. Floquet's method analysis was employed for the analyses and simulations of the antenna element in the array or achieving active parameters. Fig. 9 delineates that active impedance of the antenna is also acceptable and the performance of the antenna will not degrade even for large scanning angles. Thus, the antenna performance in the array is likewise commendable.

The simulated linearly polarized realized gains, efficiencies, and half-power beamwidth (HPBW) of the antennas are illustrated in Fig. 10. Furthermore, the simulated and measured scattering parameters are presented. This Fig. indicates that antenna D has a wider frequency bandwidth but demonstrates diminished efficiency at mid-range frequencies due to its thin and simplified design, along with direct feeding to the radiating patches for manufacturing convenience, without a coupled-line feeding mechanism. It also prepares an acceptable realized gain for the test and assessment. The simulation results of the isolation of

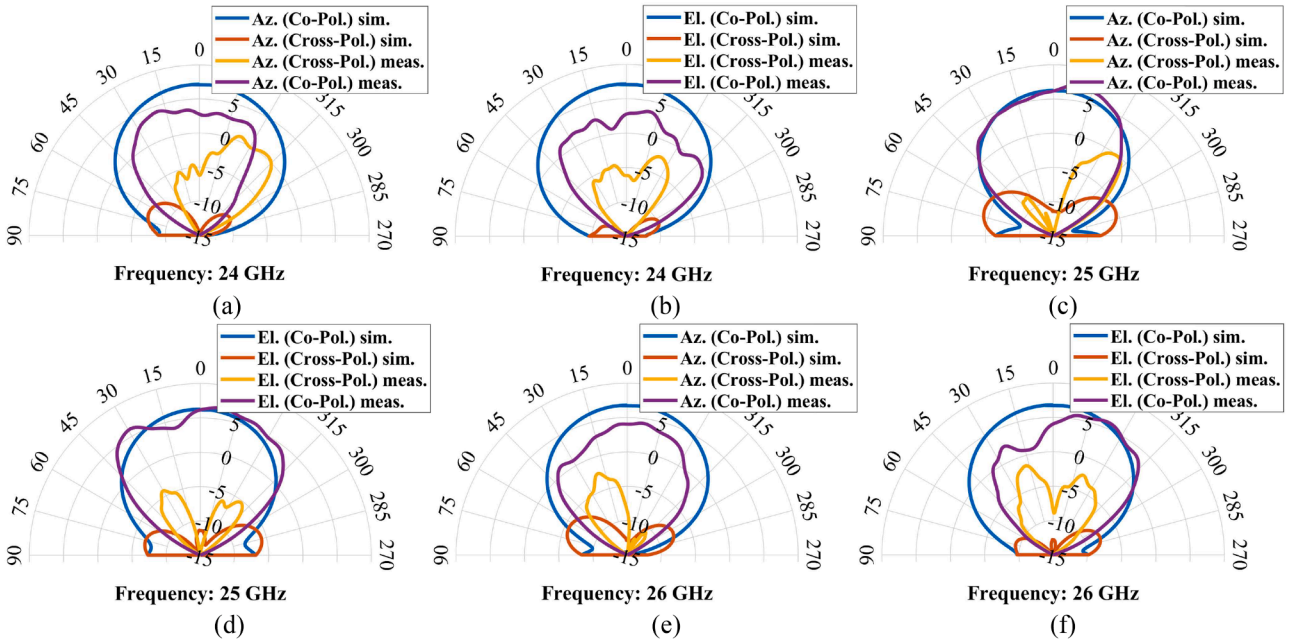

Fig. 15. Simulated and measured co-/cross-polarization realized gain radiation for circularly-polarized mode in different frequencies for antenna D.

the antenna differ from the measured values due to the fact that, as mentioned before, the isolation between the terminals of the hybrids is approximately 10 dB. Additionally, any connection lines from the output ports of the hybrids to the input ports of the antenna generate coupled signals that can transmit to all other ports.

Fig. 11 shows the simulated circularly-polarized realized gains and efficiencies and HPBW for antennas A, B, C; and simulated and measured axial ratios, and measured results of the linearly and circularly polarized realized gains for antenna D. Also, Fig. 12 illustrates the axial ratio beam patterns of the designed antennas and delineates that antennas A and B can cover the entire scanning angles without the degradations of axial ratios. Axial ratio values and radiation specifications of the antennas C, D are almost the same. Fig. 13 illustrates simulated isolation values between co-polarization and cross-polarization radiation patterns of antenna B, surpassing 80 dB. Figs. 14-15 depict the simulated and measured co/cross polarization radiation patterns of antenna D for linearly and circularly polarized modes. The elevated cross polarization values seen in the measured findings are attributed to insufficient isolation between hybrid ports, particularly the 90-degree hybrid, which is about -10 dB, as well as the coupling among connecting lines from the output ports of the hybrids to the input ports of the antenna and other reasons that were discussed in this section related to test procedure and antenna chamber. As mentioned, in comparison to antenna B, antenna A has bigger capacitances and, as a result, can resonate in lower frequency but with a little lower gain. Utilizing SRRs in antenna structures leads to more than 70% compactness. The airgap can be implemented in packaging process or by ball grid arrays (BGAs) which can lead to higher frequency bandwidth. Little differences between simulation results of the two ports are because of a little asymmetrical geometry of the ports. In the Figs, Az.: Azimuth (or φ=0°); El.: Elevation (or φ=90°); CP: Circularly-Polarized; LP: Linearly-Polarized; RG: Realized Gain.

A notable and beneficial feature of the proposed antenna is its ability to tune the operating frequency using MIM and/or Gap capacitors (Fig. 16). The resonant frequency can be adjusted from 40 GHz to 22 GHz by altering the diameter and/or spacing of the MIM capacitor connected to the VIAs adjacent to the edges of the antenna. It can attain 20 GHz by employing more and larger MIM and Gap capacitors. The resonant frequency is 10 GHz lower than that of a standard circular patch antenna with identical dimensions. The lumped capacitors have been used to replace these capacitances, and the new structure has been simulated, yielding the same results (Eq. 3). In addition, they be substituted with other types of capacitors, such as MOS or varactor diodes, or they be generated by (beamformer) ICs that incorporate variable capacitors. Their optimal values range from 0.1fF to 1pF. The simulation results are presented here due to the previously noted limitations of manufacturing technology. Fig. 16f incorporates the simulation results of the corresponding circuit model. The isolation between two differential ports is infinite in the circuit model due to the differential feeding mechanism of the antenna.

The thickness of the metal also influences the operating frequency of the antenna, and the antenna will resonate at a lower frequency when equipped with thicker feeding lines. For example, an increase in metal thickness in feeding lines from 0.01 mm to 0.05 mm will lead to a reduction of 1 GHz in the resonant frequency of the proposed antenna, which has a center frequency of 25 GHz. This is due to the fact that increased metal thickness corresponds to elevated capacitances. The proposed antenna effectively suppresses out-of-band frequency signals, as indicated by the Figs (filtering capability). To decrease the antenna dimensions to below 75% of the current sizes (antennas A, B), alternate Glass substrates with ε_r: $5 \sim 6$ can also be utilized. Thus, the antennas will have dimensions of roughly $0.2\lambda_0 \times 0.2\lambda_0 \times 0.02\lambda_0$ albeit at the expense of less efficiencies and realized gains. The unique differential-fed mechanism and the design of the proposed low-profile SRR-MD antenna make it independent of electrical permittivity. In other types of antennas, by increasing ε_r, we expect much less efficiency and realized gain. An SRR-MD antenna, designed using the conventional dimensions of a circular patch antenna and employing these structures ($\varepsilon_r = 6$), has achieved an efficiency of 85% and a realized gain of 5.5 dB. Moreover, the geometrical dimensions of the suggested antenna are comparable to those of the typical ESAs that were investigated in Section 2.2. Table I and Fig. 17 compare the current work with the previous designs in the references. Due to the SatCom applications of the antenna, its array analysis and temperature dependency are also investigated as well. Fig. 18 (a, b) depicts the elevation and azimuth radiation patterns of the 1024-element rectangular array antenna, incorporating the suggested antenna elements and employing excitation tapering to get 20 dB side lobe levels (SLLs). The uniform radiation patterns and wide horizontal and vertical HPBW of the designed antenna prevent the creation of squint angles, except at exceptionally wide scanning angles (80°), when the precise amplitudes and phases are applied. Also, temperature

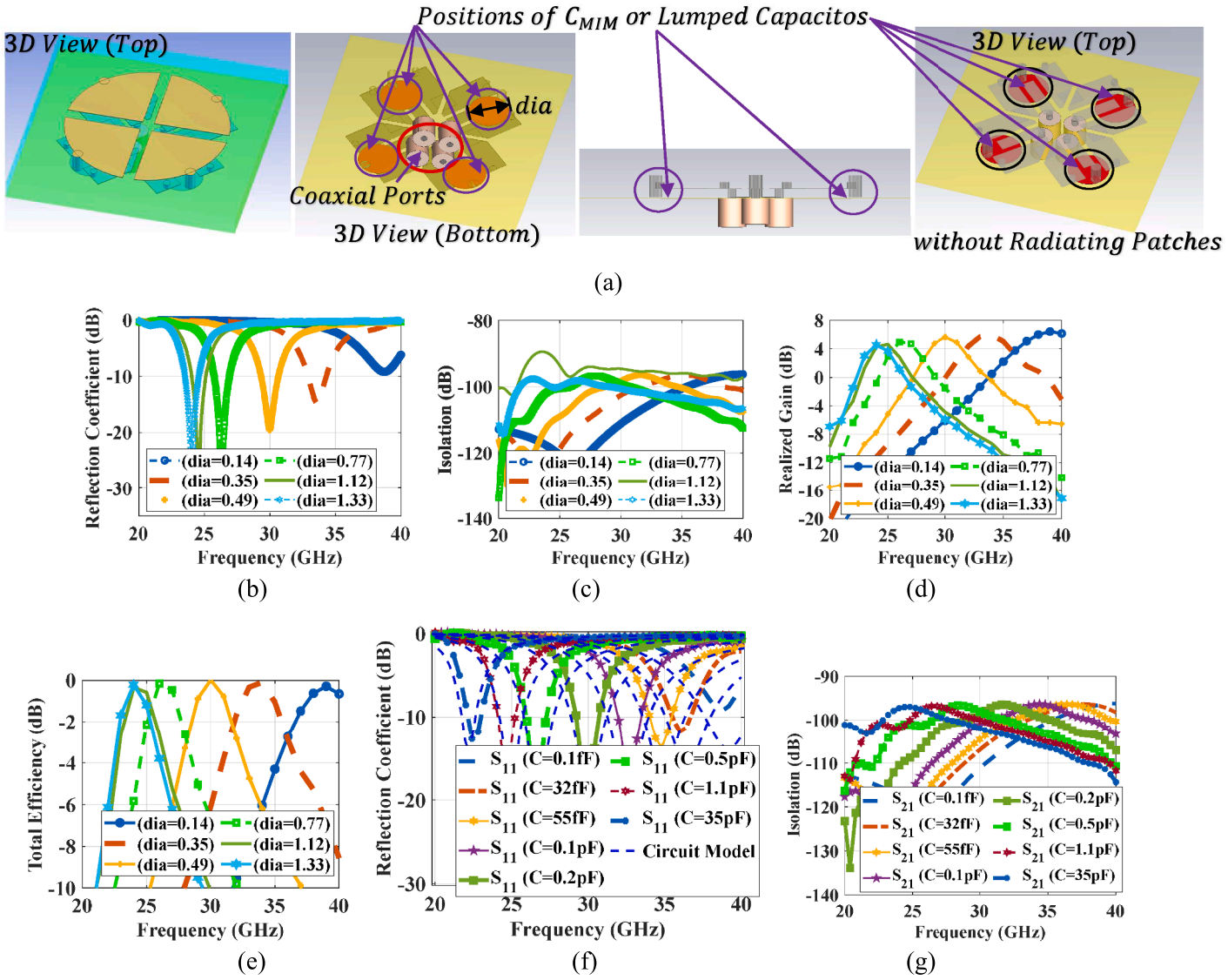

Fig. 16. a-e) Frequency sweep by changing the diameter of MIM capacitor(s) with center frequency of 30 GHz; f, g) frequency sweep by lumped element capacitors with simulation results of the equivalent circuit model.

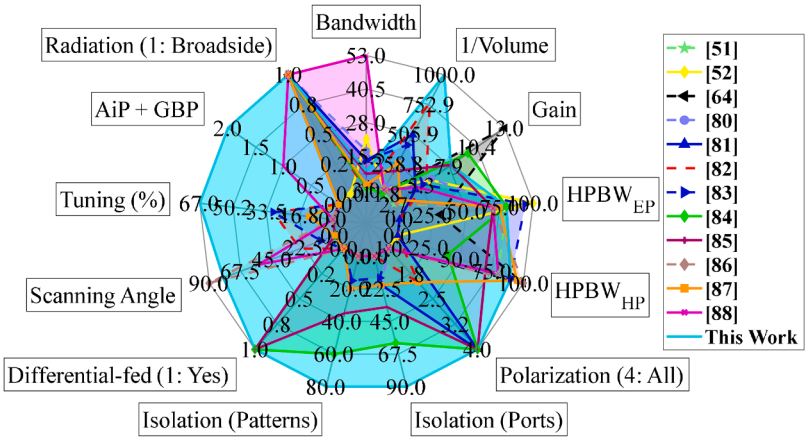

Fig. 17. Comparison of current work with previous designs (refer to Table I).

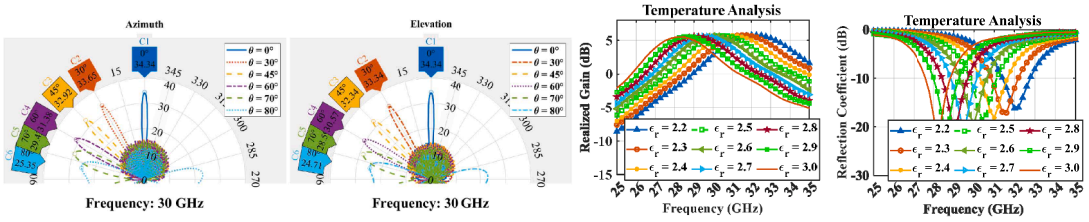

Fig. 18. a, b) Angle scanning of the proposed antenna; c, d) the temperature dependency of the antenna specifications of the proposed antenna resonating at f = 30 GHz.

variations (-50°C~160°C) influence the dielectric constant and loss tangent of substrates, as indicated by references [76–79]. Substrates like Glass and Rogers exhibit negligible variations in loss tangent. A decrease in realized gain from 6 dB to 3 dB will occur due to a rise in the loss tangent of other common substrates, such as FR4 or those with $\varepsilon_r = 2.6$ from 0.002 to 0.05.

The cited literature demonstrate that for Rogers and Glass substrates, variations in dielectric constant are approximately 1-2%, leading to an insignificant resonance shift of 0.2 GHz for the proposed antenna resonating at 30 GHz under ambient temperature conditions. However, variations in electrical permittivity must be taken into account for particular substrates that experience greater fluctuations with temperature changes. Fig. 18 (c, d) illustrates the variations in realized gain and reflection coefficient of the proposed antenna for a substrate exhibiting a 30% alteration in electrical permittivity, resulting in a 4 GHz frequency shift (28GHz-32 GHz). The center frequency of the antenna varies linearly with a slope of approximately $-5\varepsilon_r$ (f ≈ - – $5\varepsilon_r$+43).

A compact, low-profile antenna with minimal volume and broadside radiation, with a size comparable to an IC and dual differential feeding, is appropriate for AiP glass-based packaging. The suggested antenna is the most compact and low-profile design, exhibiting broadside radiation and high gain. It encompasses the whole K/Ka frequency band with a maximum frequency tuning range of 67%, incorporates filtering capabilities, and is dual differential-fed to accommodate all polarizations. AiP solutions that are low-cost require the smallest antenna configurations; however, they have been implemented at frequencies exceeding 60 GHz. The antenna demonstrated is compatible with lower frequencies due to its innovative design (0.3 mm). The proposed antenna offers excellent gain, efficiency, extensive circularly-polarized scanning capabilities, cost-effectiveness, robust shielding that prevents surface waves and superior isolation between ports and linearly polarized radiation patterns compared to similar designs.

4. Conclusion

This paper presents a new two-layer compact low-profile dual differential-fed K/Ka band SRR-MD antenna, which has been validated using simulations, comprehensive analysis, calculations, and measurements. The antenna structure has been specifically designed for integration and stacking with ICs and is appropriate for low-profile configurations, such as glass-based packaging. It does not require conventional advanced packaging and fabrication techniques employed for AiP implementation, such as LTCC or wafer-level packaging and is suitable for the entire K/Ka frequency bands. It offers superior isolation, the broader frequency-tuning capabilities with minimal volume relative to alternative designs, and facilitates high-performance broadside radiation patterns. The antenna also facilitates the wider circularly-polarized scanning angles based on axial ratio beam patterns, active parameters and measurements. It also demonstrates filtering capability and resonates at a frequency that is 10 GHz lower than that of a conventional circular patch antenna. To our knowledge, it is the most compact and low-profile dual differential-fed antenna that accommodates UWB-frequency tuning and circularly polarized scanning capabilities.

CRediT authorship contribution statement

Amir Reza Dastkhosh: Writing – original draft, Software, Methodology, Formal analysis, Data curation, Conceptualization. **Zhong-Xiang Zhang:** Supervision, Data curation. **Mehdi Naseh:** Writing – original draft, Investigation, Formal analysis. **Véronique Moeyaert:** Writing – original draft, Supervision. **Fujiang Lin:** Writing – original draft, Supervision, Conceptualization.

Declaration of competing interest

The authors declare that they have no known competing financial interests or personal relationships that could have appeared to influence the work reported in this paper.

Acknowledgements

The first author would like to thank Dr. Zhang Liang of the Anhui Normal University for his help and the measurement supports. The first author is especially grateful to Chinese Academy of Sciences and China Scholarship Council for their financial support for his PhD program.

Data availability

Data will be made available on request.

References

[1] J. Cao, et al., Toward industrial metaverse: age of information, latency and reliability of short-packet transmission in 6G, IEEe Wirel. Commun 30 (2) (2023) 40–47.
[2] L. Mohjazi, B. Selim, M. Tatipamula, M.A. Imran, The journey toward 6G: A digital and societal revolution in the making, IEEE Internet Things Mag. 7 (2) (2024) 119–128.
[3] O. Liberg, et al., Introducing 5G Advanced, IEEE Commun. Stand. Mag. 8 (1) (2024) 52–57.
[4] Massimo Mariello, et al., Wireless, battery-free, and real-time monitoring of water permeation across thin-film encapsulation, Nat. Commun 15 (1) (2024).
[5] R. Liebhart, M. Shafi, H. Tataria, G. Shivanandan, D. Chandramouli, Perspectives on 6G architectures, IEEe Wirel. Commun 32 (1) (February 2025) 108–114.
[6] A. Hazra, et al., 6G-enabled ultra-reliable low latency communication for industry 5.0: challenges and future directions, IEEE Commun. Stand. Mag. 8 (2) (2024) 36–42.
[7] M.S. Akbar, Z. Hussain, M. Ikram, Q.Z. Sheng, S. Mukhopadhyay, On challenges of sixth-generation (6G) wireless networks: A comprehensive survey of requirements, applications, and security issues, J. Netw. Comput. Appl. (2024) 104040. –104040.
[8] Amir Reza Dastkhosh, Mehdi Naseh, Davide Dardari, F. Lin, TV-based phased array system design in BTSs for 5G/IoT applications, Prog. Electromagn. Res. C 127 (2022) 1–16.
[9] P. Srividya, S. Ramya, Anitha Peram, A. Singh, Digital Convergence in Antenna Design, John Wiley & Sons, 2024.
[10] G. Maral, M. Bousquet, Satellite Communications Systems, John Wiley & Sons, 2011.
[11] R. Agasti, D.C. Nichols, A.M. Eck, H.H. Sigmarsson, J.E. Ruyle, Varactor-tuned superstrate-loaded antenna and Filtenna for X-band applications, IEEe Trans. Antennas. Propag 72 (10) (2024) 7651–7663.
[12] R. Kumari, R. Agarwal, M.K. Sharma, V.K. Tomar, Metamaterial-inspired multi-port tunable THz antenna with self-multiplexing and MIMO capability for 6G wireless and sensing applications, Braz. J. Phys. 55 (2) (2025).
[13] M. Li, S. Cheung, Isolation enhancement for MIMO dielectric resonator antennas using dielectric superstrate, IEEe Trans. Antennas. Propag 69 (7) (2021) 4154–4159.
[14] L.K. Dewangan, N.K. Mishra, Isolation enhancement of MIMO dielectric antenna using ε-negative metamaterial dielectric superstrate for NR-78 band, IEEE Trans. Dielectr. Electr. Insul. (2025) 1. –1.
[15] M. Li, B.G. Zhong, S.W. Cheung, Isolation enhancement for MIMO patch antennas using near-field resonators as coupling-mode transducers, IEEe Trans. Antennas. Propag 67 (2) (2019) 755–764.
[16] N. Collaert, New Materials and Devices Enabling 5G Applications and Beyond, Elsevier, 2024.
[17] U. Pfeiffer, et al., A 60GHz radio chipset fully-integrated in a low-cost packaging technology, in: 56th Electronic Components and Technology Conference 2006, San Diego, CA, USA, 2006, p. 4.
[18] S. Beer, H. Gulan, C. Rusch, T. Zwick, Integrated 122-GHz antenna on a flexible polyimide substrate with flip chip interconnect, IEEe Trans. Antennas. Propag 61 (4) (2013) 1564–1572.
[19] M. Swaminathan, et al., Glass packaging for 6G applications, in: IEEE Microwave Magazine, 26, 2025, pp. 46–64.
[20] X. Gu, D. Liu, B. Sadhu, Packaging and antenna integration for silicon-based millimeter-wave phased arrays: 5G and beyond, IEEe J. Microw 1 (1) (2021) 123–134.
[21] Duixian Liu, Yueping Zhang, Antenna-in-package technology and applications, Wiley-Ieee Press, Hoboken, New Jersey, 2020.
[22] T. Deng, et al., High-gain and High-efficiency sub-terahertz antenna-on-chip with microbumps for highly-integrated systems, IEEe Trans. Antennas. Propag 72 (5) (2024) 4107–4115.
[23] D. Liu, X. Gu, C.W. Baks, A. Valdes-Garcia, Antenna-in-package design considerations for ka-band 5G communication applications, IEEe Trans. Antennas. Propag 65 (12) (2017) 6372–6379.
[24] Z. Zhao, et al., A K-band fully-integrated Multi-channel active antenna-in-package module in low-temperature cofired ceramic, IEEe Trans. Antennas. Propag 73 (7) (2025) 4957–4962.
[25] T. Yu, D. Yu, Electrical performance characterization of glass substrate for millimeter-wave applications, J. Mater. Sci. Mater. Electron. 34 (2) (2023).
[26] M. ur Rehman, S. Ravichandran, A.O. Watanabe, S. Erdogan, M. Swaminathan, Characterization of ABF/Glass/ABF substrates for mmWave applications, IEEE Trans. Compon. Packag. Manuf. Technol. 11 (3) (2021) 384–394.
[27] T. Chaloun, et al., RF glass technology is going mainstream: review and future applications, IEEe J. Microw 3 (2) (2023) 783–799.
[28] M.N. Abbasi, et al., Design and optimization of a transparent and flexible MIMO antenna for compact IoT and 5G applications, Sci, Rep 13 (1) (2023).
[29] A.O. Watanabe, et al., Ultrathin antenna-integrated glass-based millimeter-wave package with through-glass vias, IEEe Trans, Microw, Theory, Tech 68 (12) (2020) 5082–5092.
[30] T.-H. Lin, et al., Broadband and miniaturized antenna-in-package (AiP) design for 5G applications, IEEe Antennas, Wirel, Propag, Lett 19 (11) (2020) 1963–1967.
[31] Y. Zhang, et al., High precision epidermal radio frequency antenna via nanofiber network for wireless stretchable multifunction electronics, Nat, Commun 11 (1) (2020).
[32] Mohammadreza Rohaninezhad, Meysam Jalali Asadabadi, Changiz Ghobadi, Javad Nourinia, Design and fabrication of a super-wideband transparent antenna implanted on a solar cell substrate, Sci, Rep 13 (1) (2023).
[33] Y. Wang, S.-W. Qu, Dual-polarized conformal transparent antenna array with hemispherical beam coverage, IEEe Antennas, Wirel, Propag, Lett 22 (10) (2023) 2452–2456.
[34] X. Gu, et al., Antenna-in-package integration for a wideband scalable 5G millimeter-wave phased-array module, IEEE Microw. Wirel. Compon. Lett. 31 (6) (2021) 682–684.
[35] S.V. Yadav, et al., Miniaturized UWB antenna design for 5G and space-based microwave applications, Results, Eng (2025) 105592. –105592.
[36] Z.-L. Su, K.W. Leung, K. Lu, Low-profile phased array antenna with wide steering range for vehicular communications, IEEe Trans, Veh, Technol 73 (9) (2024) 12305–12314.
[37] M. Hussain, W.A. Awan, S.M. Abbas, Y. Zhu, Design and development of low-profile polymer based broadband antenna for on-body applications, Results, Eng 25 (Mar. 2025) 103818.
[38] L. Lançon, et al., Integrated-transformer-based impedance matching method: impedance matching with transformers, IEEE Microw. Mag. 23 (9) (2022) 40–56.
[39] L. Li, S. Cheng, N. Mei, Z. Zhang, A well-matched and balanced impedance matching method utilizing a full-scalable magnetic-electric coupled transformer model, J. Infrared Millim. Terahertz Waves 43 (1–2) (2022) 71–93.
[40] M. Li, K.-M. Luk, A differential-fed UWB antenna element with unidirectional radiation, IEEe Trans, Antennas, Propag 64 (8) (2016) 3651–3656.
[41] Y. Zhang, Differential Antennas, John Wiley & Sons, 2024.
[42] L.J. Chu, Physical limitations of omni-directional antennas, J. Appl, Phys 19 (12) (1948) 1163–1175.
[43] H.A. Wheeler, Fundamental limitations of small antennas, Proc. IRE 35 (12) (1947) 1479–1484.
[44] J. Volakis, C.-C. Chen, K. Fujimoto, Small Antennas:Miniaturization Techniques & Applications, McGraw Hill Professional, 2009.
[45] T.V. Hansen, O.S. Kim, O. Breinbjerg, Stored energy and quality factor of spherical wave functions–in relation to spherical antennas with material cores, IEEe Trans, Antennas, Propag 60 (3) (2012) 1281–1290.
[46] C. Pfeiffer, Fundamental efficiency limits for small metallic antennas, IEEe Trans, Antennas, Propag 65 (4) (2017) 1642–1650.
[47] M. Shahpari, D.V. Thiel, Fundamental limitations for antenna radiation efficiency, IEEe Trans, Antennas, Propag 66 (8) (2018) 3894–3901.
[48] O.S. Kim, Rapid prototyping of electrically small spherical wire antennas, IEEe Trans, Antennas, Propag 62 (7) (2014) 3839–3842.
[49] S.R. Best, Low Q electrically small linear and elliptical polarized spherical dipole antennas, IEEe Trans, Antennas, Propag 53 (3) (2005) 1047–1053.
[50] J.M. Kovitz, Y. Rahmat-Samii, Using thick substrates and capacitive probe compensation to enhance the bandwidth of traditional CP patch antennas, IEEe Trans, Antennas, Propag 62 (10) (2014) 4970–4979.
[51] C.-T.M. Wu, J.H. Choi, H. Lee, T. Itoh, Magnetic-current-loop-induced electric dipole antenna based on substrate integrated waveguide cavity, IEEe Antennas, Wirel, Propag, Lett 13 (2014) 519–522.
[52] W.-H. Zhang, et al., Low-profile broadband vertically polarized microstrip magnetic dipole antenna with endfire radiation, in: IEEE Antennas and Wireless Propagation Letters, 20, 2021, pp. 2003–2007.
[53] S.K. Sharma, A. Gupta, R.K. Chaudhary, Epsilon negative CPW-fed zeroth-order resonating antenna with backed ground plane for extended bandwidth and miniaturization, IEEe Trans, Antennas, Propag 63 (11) (2015) 5197–5203.
[54] G. Jiang, et al., Abnormal beam steering with kirigami reconfigurable metasurfaces, Nat, Commun 16 (1) (2025).
[55] L. Li, Y. Shi, Tie Jun Cui, Electromagnetic Metamaterials and Metasurfaces, Springer Nature, 2024.
[56] W. Lin, R.W. Ziolkowski, Electrically small, low-profile, Huygens circularly polarized antenna, IEEe Trans, Antennas, Propag 66 (2) (2018) 636–643.
[57] N. Khiabani, et al., Metamaterial-enabled ultrawideband mmWave antenna-in-package using heterogeneously-integrated silicon IPD and HDI-PCB for B5G/6G applications, IEEe J. Emerg, Sel, Top, Circuits, Syst 14 (1) (2024) 7–18.
[58] C.A. Balanis, Antenna theory analysis and design, New Jersey Wiley, Hoboken, 2016.
[59] Balanis, Balanis' Advanced Engineering Electromagnetics, Wiley-Blackwell, 2023.

[60] Zhi Ning Chen, Springerlink, Handbook of Antenna Technologies, Online Service, Springer Singapore, Singapore, 2019.
[61] J.-S. Hong, Microstrip filters for RF/microwave applications, Wiley, Hoboken, N.J., 2011.
[62] G.H. Sosa, *Electrical modeling and optimization of multilayer via transitions for fully-integrated systems*. Diss. Doktora Tezi, National Institute for Astrophysics, Optics and Electronics (INAOE), Elektronik Bölümü, Tonantzintla, Puebla, 2011.
[63] J.D. Baena, et al., Equivalent-circuit models for split-ring resonators and complementary split-ring resonators coupled to planar transmission lines, IEEe Trans, Microw, Theory, Tech 53 (4) (2005) 1451–1461.
[64] Z. Liang, et al., Low-cost and high-gain microstrip magnetic dipole antenna with all-metal structure and open-ended stubs, IEEe Trans, Antennas, Propag 69 (6) (2021) 3543–3548.
[65] Y. Shi, J. Liu, Investigation of a via-loaded microstrip magnetic dipole antenna with enhanced bandwidth and gain, IEEe Trans, Antennas, Propag 67 (7) (2019) 4836–4841.
[66] B.J. Xiang, X. Dai, K.-M. Luk, A wideband 2-bit transmitarray antenna for millimeter-wave vehicular communication, IEEe Trans, Veh, Technol 71 (9) (2022) 9202–9211.
[67] T. Li, W. Dou, Substrate integrated waveguide 3 dB directional coupler based on air-filled vias, Electron, Lett 53 (9) (Mar. 2017) 611–613.
[68] M.J. Tavakoli, A.R. Mallahzadeh, Wideband directional coupler for millimeter wave application based on Substrate integrated waveguide, Emerg. Sci. J. 2 (2) (2018).
[69] J. Shao, R. Zhou, C. Chen, X.-H. Wang, H. Kim, H. Zhang, Design of a wideband balun using parallel strips, IEEE Microw. Wirel. Compon. Lett. 23 (3) (2013) 125–127.
[70] https://www.mtlpcb.com/en/jishu/.
[71] T.K. Sarkar, M. Salazar-Palma, Ming Da Zhu, H. Chen, Modern Characterization of Electromagnetic Systems and its Associated Metrology, John Wiley & Sons, 2021.
[72] J. Lu, W. Wang, X. Wang, Y. Guo, Active Array Antennas for High Resolution Microwave Imaging Radar, Springer Nature, 2023.
[73] Y. Fang, Y.P. Zhang, On surface-wave suppression of differential circular microstrip antennas, IEEe Antennas, Wirel, Propag, Lett 20 (9) (2021) 1691–1695.
[74] A.J. Kogon, C.D. Sarris, Finite-difference time-domain Modeling of periodic structures: A review of constant wave vector techniques, IEEE Antennas Propag. Mag. 64 (3) (2022) 59–70.
[75] A.K. Bhattacharyya, Phased Array Antennas, John Wiley & Sons, 2006.
[76] G.A. Eyebe, A.H. Rasolomboahanginjatovo, Benoit Bideau, F. Domingue, Investigation on temperature-dependent dielectric properties of ETFE fluoropolymer for microwave temperature sensing applications, Sens, Actuat, Phys 290 (Mar. 2019) 215–221.
[77] C.A. Nieves, Z.W. Cohick, M.T. Lanagan, M.T. Marakovits, Temperature-dependent dielectric behavior of glass substrates in the W-band for mm-wave applications, J. Am, Ceram, Soc (2025).
[78] John. Coonrod, Circuit materials and high-frequency losses of PCBs, PCB mag. 24 (2) (2012).
[79] X. He, C. Yu, Z. Liang, M. Xiao, E. Li, Dielectric and structural properties evolution of PTFE-based high-frequency circuit substrates for mmwave application under hygrothermal aging, Polym, Degrad, Stab (2025) 111192. –111192.
[80] Y. Gong, X.-L. Yang, X.-W. Zhu, Millimeter-wave filtering antenna and array with multiple flexible radiation nulls based on hybrid coupling of SIW cavities and split-ring slots, IEEe Antennas, Wirel, Propag, Lett 24 (4) (2025) 823–827.
[81] S. Liu, Z. Wang, Y. Dong, Compact wideband SRR-inspired antennas for 5G microcell applications, IEEe Trans, Antennas, Propag 69 (9) (2021) 5998–6003.
[82] Z. Wang, Y. Dong, Miniaturized RFID reader antennas based on CRLH negative order resonance, IEEe Trans, Antennas, Propag 68 (2) (2020) 683–696.
[83] Z. Wang, Y. Dong, T. Itoh, Miniaturized wideband CP antenna based on metaresonator and CRLH-TLs for 5G new radio applications, IEEe Trans, Antennas, Propag 69 (1) (2021) 74–83.
[84] Y. Luo, Z.N. Chen, K. Ma, A single-layer dual-polarized differentially fed patch antenna with enhanced gain and bandwidth operating at dual compressed high-order modes using characteristic mode analysis, IEEe Trans, Antennas, Propag 68 (5) (2020) 4082–4087.
[85] H. Huang, X. Li, Y. Liu, A low-profile, dual-polarized patch antenna for 5G MIMO application, IEEe Trans, Antennas, Propag 67 (2) (2019) 1275–1279.
[86] Z.-L. Su, K.W. Leung, K. Lu, Low-profile phased array antenna with wide steering range for vehicular communications, IEEe Trans, Veh, Technol 73 (9) (2024) 12305–12314.
[87] D. Chaturvedi, A. Kumar, A QMSIW cavity-backed self-diplexing antenna with tunable resonant frequency using CSRR slot, IEEe Antennas, Wirel, Propag, Lett 23 (1) (2024) 259–263.
[88] B. Yu, et al., A wideband mmWave antenna in fan-out wafer level packaging with tall vertical interconnects for 5G wireless communication, IEEe Trans, Antennas, Propag 69 (10) (2021) 6906–6911.

Amir Reza Dastkhosh is currently a Ph.D. student at the University of Science and Technology of China (USTC), located in Hefei, China. He obtained his M.S. in electrical engineering from Sahand University of Technology, Iran. Phased array antennas, passive devices, radar, frequency synthesizers, satellite mobile communications, optimization methods, health issues and effects of electromagnetic radiations and modelling are some of his areas of interest in research.

Mehdi Naseh is currently a Research Collaborator with the Department of Electromagnetism and Telecommunications (SET) as well as a Networking Lab member at Computer Science Department, University of Mons, Belgium, where he served as a Research Associate (all through 2024) in the field of 6 G Wireless Communications for the National Belgium 6 G project (BEL6GICA). He was a Research Fellow at the Department of Electrical, Electronics, and Information Technology (DEI), University of Bologna, Italy, in the field of Localization and Sensing (2020-2021), where he graduated in Electronic Engineering, and a former Researcher at Advanced Research Center on Electronic Systems (ARCES), Italy in the field of Energy Harvesting for Internet of Things (2021-2023). In addition to having more than eight years of teaching experience, he is the main author of two books in Signals and Systems Analysis and Electronics (Analog). Over the past five years, he has also been on the organizing committee for several IEEE conferences and technical meetings in Belgium and Italy.

Véronique Moeyaert (Member IEEE) received the M.S. degree in Electrical Engineering and the Ph.D. degree in Applied Sciences from the Faculté Polytechnique de Mons (FPMs), Belgium, in 1993 and 2002. Since 2013, she has been a Professor in Telecommunications at the Université de Mons (UMONS), Belgium. She has her main research interests in the physical layer performance estimation and optimization of optical, electrical, and wireless transmission systems, either analogue or digital. Particularly, she is working on HFC networks, RoF systems, industrial & LPWAN IoT systems, VLC communications in the frame of smart cities, and PLC systems for both the power grid and railway signalling.

Fujiang Lin (Senior Member, IEEE) received the BSc and MSEE degrees in Radio Physics and Microwave Antenna from the University of Science and Technology of China (USTC), Hefei, China, and the Dr.-Ing. degree in MMIC from the University of Kassel, Germany. Dr. Lin has been tenure full time professor at USTC since 2010. He established the USTC Exceptional School of Microelectronics after Micro/nano-Electronic System Integration R&D Center (MESIC) focusing on advanced nanotech devices modelling and IC design. His current research interests are mmWave digital phased array antenna μSys integration, opto-electronic IC for ultrahigh-speed Ethernet, GaN based 3rd generation device ASM-HEMT modelling cum MMIC design and start-up entrepreneurship. Prior returning back USTC, Dr. Lin worked as SMTS and PI in the Institute of Microelectronics (IME), A*STAR, Singapore; as adjunct Associate Professor at NUS; as Director in CHRT (now GlobalFoundries); as Technical Director at HP/Agilent (now Keysight) EEsof; as founder and CEO of Transilica Singapore. Professor Lin actively involved in varies IEEE activities, including IEEE Singapore MTT-S/APS jointed Chapter Chair, IEEE RFIC EdCom, Advisor for IEEE R10, Mentor for USTC-SSCS Student Branch Chapter; Board reviewer member for T-MTT, TCAS, TTHZ etc, TPC member for IMS, RFIC, EuMC, APMC etc. Co-founder for IEEE RFIT and IEEE ICTA. Dr. Lin has extensive hand-on and multi-discipline experiences and knowledge in advanced micro-/nano-electronics technologies, as well as the related integrated circuits and package modelling cum system co-design. Prof. Lin has trained up over 170 postgraduate students, published over 300 peer-reviewed papers and over 90 patents.